28th EUROPEAN ROTORCRAFT FORUM

Bristol, England - September 17-20, 2002

Paper 42

The HART II test in the LLF of the DNW - a Major Step towards Rotor Wake Understanding

Berend G. van der Wall, Bernd Junker, DLR Braunschweig, Germany
Casey L. Burley, Thomas F. Brooks, NASA Langley, USA
Yung Yu, Chee Tung, US Army AFDD, USA
Markus Raffel, Hugues Richard, Wolfgang Wagner, DLR Göttingen, Germany
Edzard Mercker, Kurt Pengel, Hermann Holthusen, DNW, Netherlands
Philippe Beaumier, Yves Delrieux, ONERA, France

The HART program of 1994 led to deep insight into the effect of HHC on rotor behavior and its noise radiation. A key parameter to reduce rotor noise by HHC is the wake location relative to the blades. Wake data, however, had only been very scarse in HART, which was related to the flow measurement technique available at that time: 3C-LDV which provided conditionally averaged data by a relatively time consuming pointwise measurement in space. During the data analysis in the years after HART it was found that essentially comprehensive wake data are needed in order to get insight into wake development, vortex creation and aging, their motion in space and time and their re-development after an interaction with a rotor blade. Therefore, DLR, ONERA, NASA Langley, US Army AFDD and DNW again came together and created a follow-on program named HART II. The main focus was aiming on the rotor wake, which was investigated by the intensive use of a novel double stereo PIV system consisting of six laser oscillators and five digital cameras mounted on a large common traversing system. This provides instantaneous flow field data in both a large observation area and in a smaller close-up view to the vortex core. Additionally, rotor dynamics, aerodynamics, and noise radiation were subject of investigation to form a complete, consistent, and comprehensive data base. Another "first time" was the blade position measurement technique SPR (Stereo Pattern Recognistion) which provides instantaneous optical measurement of the blade bending in flap, lead-lag and torsion. In this paper, the HART II test is described in detail, with all measurement techniques applied and with some results from each of them.

Nomenclature

Abbreviations

AFDD	Aeroflightdynamics Directorate
BL	Baseline case
BTD	Blade Tip Deflection
BVI	Blade Vortex Interaction
DNW	German-Dutch Wind tunnel
HART	HHC Aeroacoustic Rotor Test
HHC	Higher Harmonic Control
LDV	Laser Doppler Velocimetry
LLF	Large Low-speed Facility
LLS	Laser Light Sheet
MoA	Memorandum of Argeement
MoU	Memorandum of Understandment
MN	Minimum Noise case
MV	Minimum Vibration case
NASA	National Aeronautics and Space Administration
ONERA	Office National D'Etudes et de Recherches Aerospatiales
PIV	Particle Image Velocimetry
SPR	Stereo Pattern Recognition
3C	Three Component

Symbols

a_∞	speed of sound, m/s
c	chord, m
C_n	normal force coefficient
C_T	thrust coefficient, $= T/(\rho\pi\Omega^2R^4)$
M_H	tip Mach number, $= \Omega R/a_\infty$
N_b	number of blades

r	radial coordinate, normalized by R
R	rotor radius, m
t	time, s
T	thrust, N
u, v, w	velocity components, m/s
V	velocity, m/s
x, y, z	coordinates, normalized by R
α	angle of attack, rad
β_0	blade cone angle, rad
ϕ	flight path angle, rad
θ	pitch angle, rad
μ	advance ratio, $= V/(\Omega R)$
ρ	air density, kg/m^3
σ	solidity, $= M_b c/(\pi R)$
ψ	azimuth, $= \Omega t$, rad
Ω	rotor rotational frequncy, rad/s
Indices	
n	n-th harmonic, n-th order
S	shaft
t	blade tip

1 Introduction

In 1994, the impact of HHC on rotor aerodynamics, dynamics, and noise emission were deeply investigated within the HART test [1]. Therein it was clarified that the main effect of noise reduction due to HHC is a significantly increased blade-vortex miss-distance, even though the vortex strengths are increased compared to a conventional control situation without HHC [2, 3]. It was also found that the differences in blade motion due to HHC are about one order of magnitude smaller than the differences in vortex motion. The key parameter for noise simulation thus is the wake simulation. Significant advances were achieved using free-wake [4, 5, 6] and prescribed wake simulation [7], but very limited data exist for the voretx modeling itself, i.e. its roll-up process and behavior afterwards (velocity profile, circulation, aging processes).

Within the framework of the US/German MoU and the US/French MoA the partners of the HART program met again to create a follow-on test called HART II in order to now focus on the rotor wake and its development within the entire rotor disk [8]. This test was conducted within a three week test campaign in October 2001 in the LLF of the DNW. A total amount of 63000 3C-PIV data sets had been taken, 33600 SPR and BTD data sets, 183 rotor and balance data sets, 642 noise measurements, 157 pressure data sets. In total roughly a TeraByte (1TB = 1000GB) of raw data did exist after the test.

Prior to the test, a prediction team was established with members from NASA, US Army, ONERA and DLR in order to predict the wake vortex locations at the areas of intended measurement. These predicted results were utilized during testing to locate the PIV traverse and were found to significantly accelerate the PIV measurement procedure during the test.

Variable	nominal value
V	33m/s
rpm, Ω	1041, 109rad/s
μ	0.15
M_t	0.641
C_T	4.4e-3
$C_{Mx} = C_{My}$	0.0
α_S	5.3^o
BL:	$\theta_3 = 0.0^o$
MN:	$\theta_3 = 0.8^o$, $\psi_3 = 300.0^o$
MV:	$\theta_3 = 0.8^o$, $\psi_3 = 180.0^o$
α_S-sweep:	-6.9^o, -3.8^o, -0.7^o, 2.3^o, 11.4^o
HHC phases:	$\psi_3 = 0^o$, ..., 330^o; $\Delta\psi_3 = 30^o$

Table 1: Basic conditions in HART II.

Due to an accident in a preceding test the Bo105 model rotor used during the HART test of 1994 was not available. An existing uninstrumented Bo105 model rotor was thus upgraded with 51 absolute pressure transducers for the HART II test. However, the rotor, although designed for the same fundamental frequencies in flap, lead-lag and torsion, had different behaviour in torsion due to a different design of the main spar and the location of the elastic and the center of gravity axis. This different behavior was the reason to again verify the conditions of the HART test in HART II by repeating the acoustic measurements, including the HHC phase sweep at 3/rev control.

Main emphasis was put on the baseline case of HART plus the α-sweep of it, and the two HHC cases with settings for minimum vibration and minimum noise radiation. Tab. 1 provides an overview of the fundamental conditions. Therefore, HART II was designed to extend the data base of HART by all the wake data missing plus the validation of the reference cases by additional measurements of the acoustics and the blade motion.

2 Test setup and workshare

2.1 Test content and workshare

For the four parts of the test different measurement equipment was needed and thus different test set-ups were erected, while the rotor rig remained the same for the entire program. The various parts of the test are given in Tab. 2 and

Part	Content
I	Noise radiation: α-sweep, 3/rev HHC phase sweep
II	PIV advancing side: BL, MN, MV, α-sweep
III	PIV retreating side: BL, MN, MV, α-sweep
IV	Blade position: BL, MN, MV, α-sweep

Table 2: Test content of HART II.

Measurement	method
noise emission	microphones: DNW
blade pressure	absolute pressure transducers: DLR
rotor data	strain gages, potentiometers: DLR
balance data	strain gages, piezo transducers: DLR
blade position	SPR and BTD: DNW
wake data	3C-PIV: DLR, DNW

Table 3: Measurements performed in HART II.

the workshare of measurements during the test is given in Tab. 3.

2.2 Rotor test rig

The rotor test rig as shown in Fig. 1 was mounted on the sting support of the wind tunnel. The rotor is driven by a hydraulic engine (green block to the left of the figure) via a transmission belt. In the rotor shaft a torque meter was implemented that measured the drive moment via strain gauges. Power and measured strains are transmitted inductively to the non-rotating part. Seven force transducers connected the balance upper plate with the test rig base, four in vertical, two in lateral and one in horizontal direction. They consisted of a strain gauge component for the steady part and a piezo material component for the dynamic part of the forces. A list of rotor properties is given in Tab. 4.

On top of the balance upper plate the swashplate actuators were mounted. They consisted of a lower electrical actuator part which was used for conventional control (collective and cyclic), while on top of them the hydraulic HHC system was positioned which was tuned for only 4/rev dynamic motion. A HHC controller was responsible for equalizing the amplitudes of all HHC actuators and to keep the proper phase relation between them. Thus, a 3, 4 and/or 5/rev control was possible in the rotating frame. However, in HART II only the 3/rev was used.

Two rotor blades were equipped with blade pitch sensors, and each of the four blades had six strain gauge pairs at the root: three for flap, two for lead-lag, and one for torsion, see Fig. 2. In total 51 absolute pressure transducers were distributed on two blades. With them the leading edge pressure distribution was measured between 40 and 97% span, and at 87% span a chordwise distribution of 17 Kulites allowed the computation of the sectional aerodynamic loading (Fig. 3). Below the hub two strain gauge pairs were mounted on the shaft for its bending moments in the rotating frame. All data from the rotating frame, i.e. 79 channels, were pre-amplified in the rotating frame and then transmitted via a slip-ring system.

Property	value
number of blades	4
radius	$2m$
root cutout	$0.44m$
chord	$0.121m$
solidity	0.077
airfoil	NACA23012
tab length	$5mm$
linear twist	$-8^o/R$
precone	2.5^o

Table 4: Properties of the model rotor.

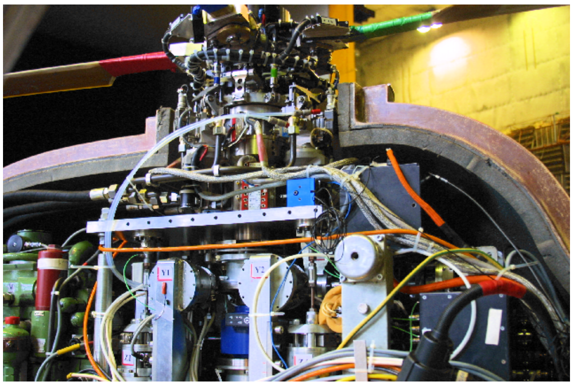

Figure 1: Rotor test rig.

2.3 Noise measurement set-up

The noise measurements were performed with 13 microphones mounted laterally on a traverse, ex-

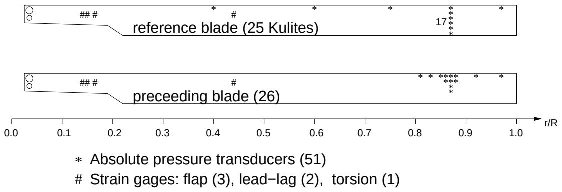

Figure 2: Instrumentation of the rotor blades.

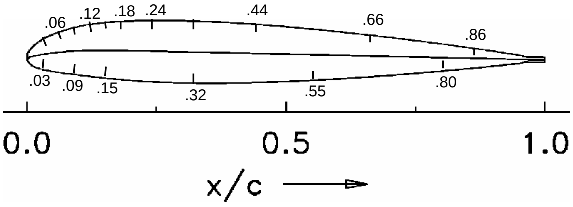

Figure 3: Chordwise distribution of pressure sensors, r/R=0.87.

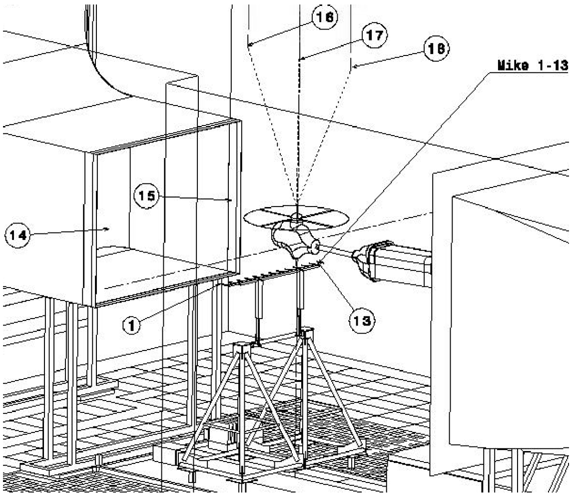

Figure 4: Test set-up for noise measurements.

tending the range of $-1.35 \leq y/R \leq 1.35$, see Fig. 4. In streamwise direction the traverse covered the range of $-2 \leq y/R \leq 2$. The vertical distance to the hub center was $1.5R$. Additionally, two microphones were located in the nozzle exit and three below the ceiling.

2.4 PIV measurement set-up

In order to cover the proposed test matrix of PIV locations, a common support was used that had three traverses (in x, y, and z direction) plus a central hinge for rotations about the vertical axis, see Fig. 5. On the lower platform the lasers of DNW and DLR were mounted, their beams were directed vertically into the flow and aligned on the same plane for maximum light energy. The camera systems were mounted on the z-traverse of the common support's vertical tower and had a range of $0.5R$, which was nearly centered on the predicted vertical range of vortex locations. The cameras were spaced vertically such that two cameras were looking from below the observation area, and the other cameras from above [9]. For measurements on the other side of the rotor disk, the entire common support was moved there and measurements could be continued without recalibration since the laser/camera setup remained unchanged.

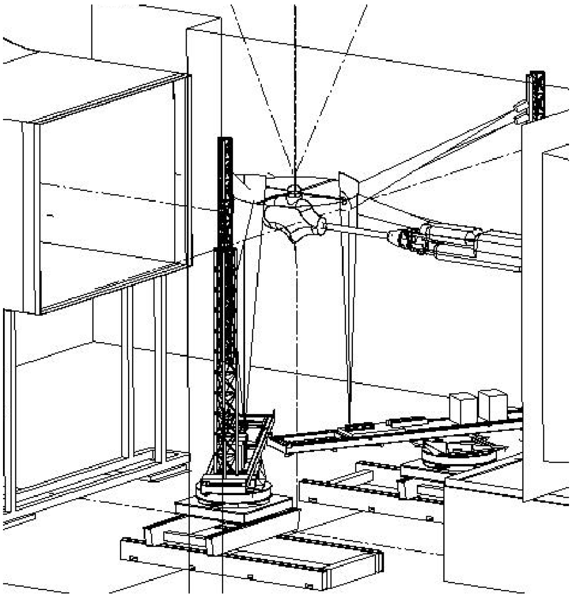

Figure 5: Test set-up for PIV measurements (two positions of the common support for measurements on advancing and retreating side).

2.5 SPR measurement set-up

The SPR and BTD measurements required four cameras widely spaced on ground. One pair of cameras focused on the advancing side of the disk, and the other one on the retreating side. In addition, the common support was used for one camera focusing on the 90^o azimuth position of the blade, and a second tower was holding another camera for a view on the 135^o position. These two cameras were focused only on the blade tip at the respective azimuth positions and measured the lead-lag, flap and torsional deflections of the tip relatively to its non-rotating position at these azimuths. The setup is schematically given in Fig. 6.

For SPR measurements the blades were painted black and equipped with white markers on the lower side. These were distributed equally all along the leading and trailing edge such that 18 radial stations were covered from $r/R = 0.223$ to 0.997, see Fig. 7. In addition, a plate with four markers was mounted below the fuselage shell and centered about the shaft axis. Its purpose was to identify the hub location during the SPR measurements. During the calibration phase a grid of markers was positioned in the rotor disk area. Each markers position was measured by means of Theodolite and the SPR cameras. This formed the basis of the mathematical model to recompute the blade marker positions in space from the two camera images in the aftermath. More details about SPR will be available in [10].

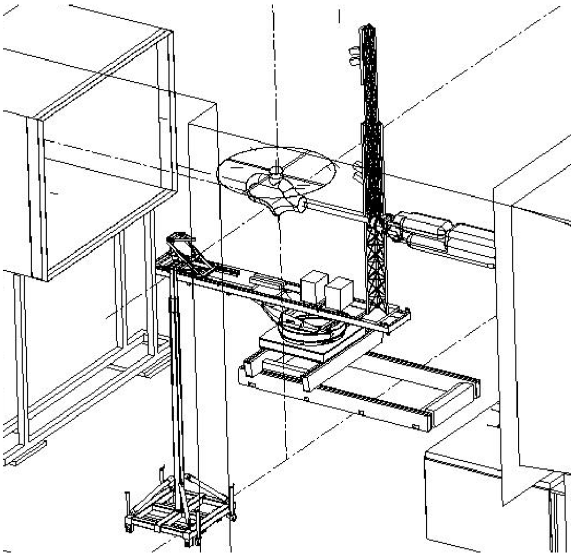

Figure 6: Test set-up for SPR and BTD measurements.

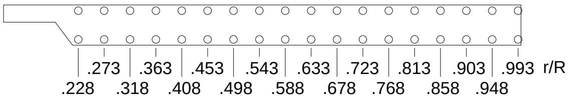

Figure 7: Distribution of SPR markers on the rotor blades.

3 Execution of HART II

3.1 General procedure

A special sequence was applied to optimize the speed of measurements. First, the wind tunnel and the rotor were put on operational condition as specified in the test matrix. Then, the wind tunnel data (air data, model position) were provided by DNW and recorded together with the rotor and balance data by DLR. Next, the blade pressures were taken immediately thereafter. Both - rotor and blade pressure data recordings - needed only a few seconds. Thereafter, the microphone measurements started, which took a few minutes due to the traversing needed. In total, this sequence took about 13 minutes per condition.

During the PIV measurements neither acoustic nor blade pressure data were recorded. After the trim of the rotor and the balance data recording for the verification of conditions, the PIV recordings were started, and an average of 5 minutes was obtained per position to be measured (with 100 PIV images taken per position and camera).

The SPR measurements were executed in the same manner, but in most cases only 50 images were taken, which shortened the measurement down to 3 minutes per position.

An overview of the total time spent for measurements and overhead is given in Fig. 8. From the 16 days of tunnel occupation time the largest amount was spent for configuration changes (acoustic measurement to PIV, from PIV to SPR) which included notable amount needed for calibration. Another big portion is the test rig assembly and dis-assembly, which includes mass balancing, tracking, some calibrations and functionality checks.

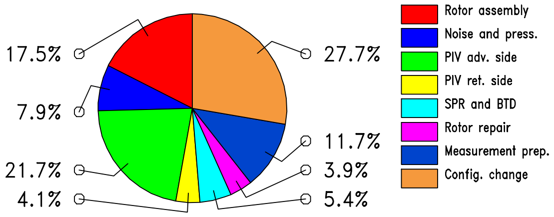

Figure 8: Components of tunnel occupation time.

However, almost 8% were spent for acoustic and blade pressure measurements, almost 26% for PIV measurements, and some 5% for SPR measurements, which sum up to almost 40% for pure measurements, which is a very good number. Repairs on the rotor and test rig covered roughly 4% of test time, which can be seen as less than normal, and repairs on measurement equipment required almost 12%, which appears to be significant. However, it must be taken into account that the measurement techniques applied were a “first” in this wind tunnel: 3C PIV in such a complex set-up as well as SPR were not done before.

3.2 Rotor and balance data

The rotor data contain the strain gage signals from every blade, two root pitch sensors, shaft bending moments and all pitch link forces. From the non-rotating frame the shaft inclination, rotor azimuth, balance forces, power, actuator force and displacements, swashplate accelerations and temperatures were measured. All of these were recorded for a duration of 32 revolutions at a sample rate of 128/rev and immediately processed for verification of condition and failure detection. They were immediately available for analysis of results. Rotor and balance data were measured at all parts of the test, in total 183 data points were taken. The data acquisition system is described is [11].

3.3 Noise measurements

Noise measurements were performed by DNW with 13 microphones on a traverse, two in the nozzle and three at the ceiling. The traverse was starting in the most upstream position ($-4m$) with a free-run mode of a fixed samle rate of

88kHz for 30 seconds, then travelling downstream in increments of $0.5m$ with a stop for measurements. At these positions the microphones were recorded for 100 revolutions continuously at a sample rate of 2048/rev (about 35.5kHz), together with the 1/rev signal of the rotor, and the data acquisition was triggered to this signal.

In the aftermath, the microphone data were processed in different ways. First, a time averaged microphone pressure time history was computed for one rotor revolution, and from this time history the spectrum was analysed. Second, for each individual revolution a spectrum was computed, and then an average spectrum from all these individual ones. The results were available shortly after the measurements and allowed a comparison with data from earlier tests for verification of the condition.

The measurements performed covered background noise, an α-sweep from 6^o climb to 6^o descent, a complete sweep of 3/rev HHC phase angles in increments of 30^o phase angle, a Reynolds effect study (which included the α-sweep at half rotational speed), a full scale comparison study (with trim from flight test), and a hover case. Additionally, simultaneous measurements of blade pressures and acoustics (at a selected traverse position) were made for 80 continuous rotor revolutions, and repeated 12 times for blade-wake interaction studies. This was again applied to the α-sweep. In total, 642 noise measurements were made.

3.4 Blade pressure measurements

During the same part of the test where noise measurements were performed also blade pressure measurements were done. After rotor data have been acquired, a data file with the tunnel and rotor operating condition was provided and the pressure measurements were started when the reference blade passed the 0^o azimuth position. At each revolution 2048 samples were taken for every sensor. All pressure transducers were recorded simultaneously for 64 revolutions and the signal quality was surveyed online. Right after the measurements the post-processing allowed access to the data for computation of C_nM^2 time histories, or leading edge pressure distribution, spectra analysis etc.. This allowed verification of conditions with former data, for example the HART test of 1994. Most of the blade pressure measurements were done ahead of the microphone measurements.

Together with the simultaneous measurements of pressures and microphones, 157 pressure measurements were made, covering the entire set of conditions described before.

3.5 Flow measurements

The flow measurement techniques available in HART 1994, did not allow for a large area of observation of the wake due to the very time consuming approach of LDV [12, 13]. Recent advances in measurement techniques made PIV mature for routine usage in rotor testing [14]. Its main advantage compared to LDV is first the small amount of time needed for the measurement itself (namely two photographs within a time of a few milliseconds), second the results are instantaneous velocity vector fields compared to conditionally averaged data from LDV, and third PIV provides a complete observation area of instantaneous data within one measurement compared to just a point in space (and time) by LDV.

Using two cameras which are focused on the same area but from different points of view the third flow velocity component perpendicular to the observation plane could be analysed in the aftermath. By means of this technology a complete field of velocity vectors in a plane observation area could be measured instantaneously, and a set of 100 data taken at each measurement location allows for a thorough statistical analysis. In HART II both DLR and DNW provided such a stereoscopic PIV system which were focused on the same central point. Different lenses led to a large observation area (DNW) of lower spacial resolution for the global flow analysis around the tip vortex of investigation. A small central observation area resulted in the DLR PIV system with high spacial resolution of the vortex core. As an example of the raw data, a typical image is shown in Fig. 9. These images were used to traverse the cameras such that their center concincides with the center of the vortical structure visible. At several locations and operating conditions this was a challenging task, especially when a widely distributed vorticity was found instead of a concentrated vortex.

The locations where measurements were intended to be performed covered the entire rotor disk, see Fig. 10. In (a) the BL case is shown at an azimuth of $\psi = 20^o$, at which the PIV locations and their numbering is given. The intention was to trace the tip vortex of the reference blade from its creation on its way downstream throughout the disk. For this purpose the trigger of the cameras had to be shifted by 90^o at each step downstream. Due to the optical arrangement with upstream view all positions in the front of the disk were hidden by the blade at $\psi = 110^o$. Thus, another reference azimuth was selected for the remaining locations, which is shown in (b) at the example of the MV case, which is known to create double vortex systems due to download at the tip in parts of the second quadrant. The list of

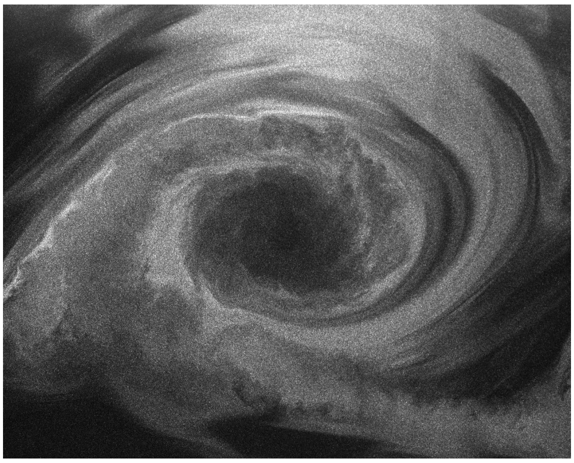

Figure 9: PIV raw data image.

$\psi/^o$	locations measured
20	8, 16, 20, 27, 32, 38, 44, 49, 53
110	5, 13, 21, 28, 29, 33, 39, 45, 50
200	6, 14, 22, 30
290	7, 15, 23, 26, 31, 37, 43, 48, 52
70	4, 35, 42
160	1, 9, 17, 24, 54, 55, 56
250	2, 10, 18, 25, 34, 40, 46, 51
340	3, 11, 35, 41, 47

Table 5: List of reference blade azimuth and related measurement locations.

reference blade azimuth and related measurement locations is given in Tab. 5.

Some special locations may be addressed here. These are 55a, where the vortex creation is measured right behind the trailing edge (vortex age 3.5^o) in increments of 5^o azimuth. Second, at 21 blade-to-blade differences were investigated: here the vortex of each blade was measured. Third, at 21a the observation angle was rotated by 90^o such that the measurement plane was in parallel to the vortex axis. In addition, at a subset of locations on the advancing side (5-7, 13-15, 20-22, 26) the entire α-sweep was measured.

The flow measurements covered most of the testing time. They were applied mainly to the BL, MN, and MV condition, which were measured completely (advancing and retreating side), and to the α-sweep, where selected locations on the advancing side were measured. In total, 315 PIV measurements were made by both of the camera systems, with 100 images taken at each of them. This makes 63000 vectors fields to be analysed, stemming from 252000 single camera images.

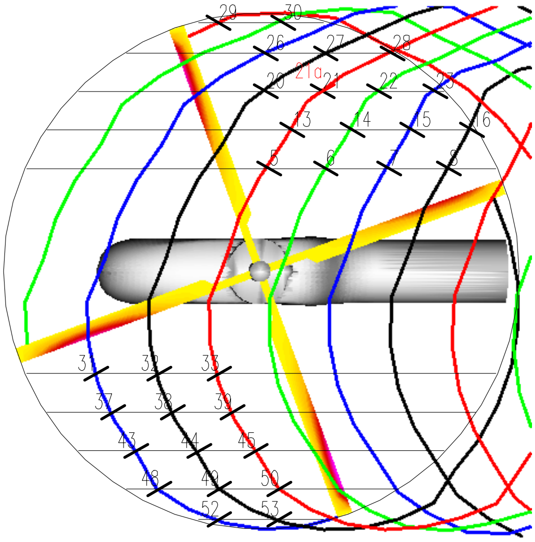

a) BL, $\psi = 20^o$

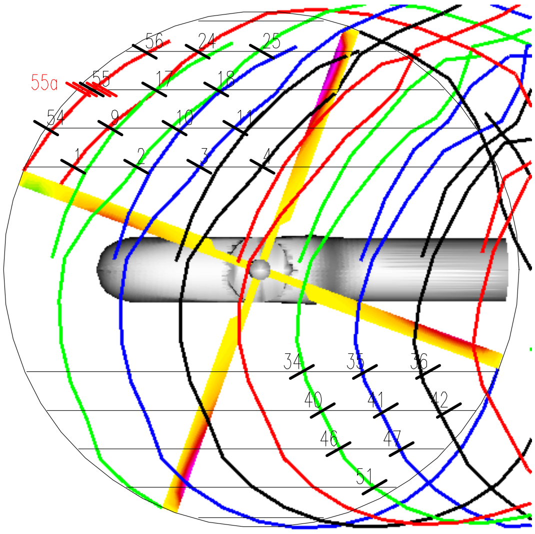

b) MV, $\psi = 70^o$

Figure 10: Locations of PIV measurements in the rotor disk.

3.6 Blade position measurements

The blade motion was measured optically by SPR technique with four floor-mounted cameras. A pair of them was focused on either half of the rotor disk such that the entire disk could be observed. All rotor blades had markers on both the leading edge and the trailing edge from 23% span up to the tip. Data were taken at 15^o azimuth increments such that the analysis allows to synthesize the lower harmonics from the time history of the blade motion over the entire length of the blade. Again, 80 to 50 data sets were taken at each location for a statistical analysis and for blade-to-blade differences.

It is worthwile to note that the analysis of the SPR raw data images mainly was identical to that of the PIV images. The position of the same markers was different in the corresponding camera pair, and with the calibration done ahead of the test the absolute positions in space were analysed. In parallel, the position of the model was

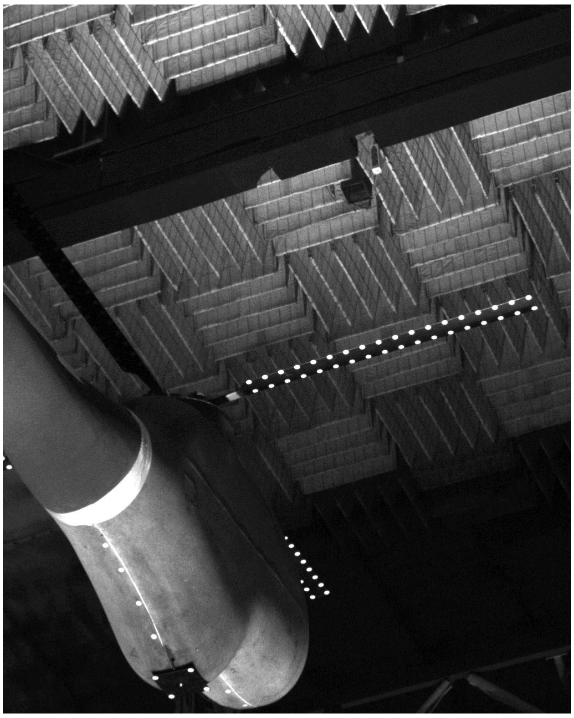

Figure 11: SPR raw data image at $\psi = 90^o$.

measured at each data point and therewith the hub center location was known. The combination of both provides the marker positions relative to the hub, which is the result needed.

An image of one SPR camera is given in Fig. 11. The blade is at a 90^o azimuth position and the markers at leading and trailing edge are clearly visible.

In parallel to SPR, two cameras were mounted on piles outside the flow which were directed on the $\psi = 90^o$ and 135^o blade position in order to independently measure the blade tip vertical, horizontal and pitch position. This setup was called BTD (blade tip deflection measurement). At these azimuth, the results of BTD can directly be used as validation of the SPR results.

SPR measurements were applied to the BL, Mn, and MV case, and to parts of the α-sweep, covering 6^o and 3^o climb and 12^o descent. At each condition 24 locations were measured around the revolution in increments of 15^o azimuth. In total, 144 SPR measurements were made, wherein 24 contain 100 repeats and the rest 50 repeats at the same location for statistical analysis. Since at each location all four blades are measured, this makes 33600 data sets of blade and body marker coordinates for post-processing. They stem from the same amount of camera raw data images.

4 Some results

4.1 Acoustic results

Noise radiation as measured in a plane $1.11R$ below the rotor hub center is shown in Fig. 12 for the range of 6^o climb (a), level flight (b), 3^o, 6^o, and 12^o descent (c-e); all at $\mu = 0.15$. The radiation of mid-frequency noise (6-40 blade passage frequency = 24-160/rev) was computed from the microphone signals of the inflow traverse. The intensity - as well as the directivity of noise radiation - is strongly depending on the flight path angle with a maximum at 6^o descent, which compares well to earlier measurements like [15, 1]. This is the reason why to apply HHC at that specific flight path angle. At 12^o descent the traverse was stopped by the sting support and thus could not reach the last two positions downstream.

HHC was applied in a way such that the root pitch amplitude was $\theta_3 = 0.8^o$ at each phase setting, which is in contrast to the HART test of 1994, where 0.8^o were commanded, but the effective root pitch amplitude was significantly larger (up to 0.87^o) and depended on the phase of the input. Additionally, the HART II rotor blade set was slightly differing from the HART blade, especially in torsion and flap-torsion coupling. As a result, smaller torsion occured in HART II and thus HHC effects are smaller compared to results from HART of 1994. This is especially visible in the noise radiation for two specific HHC settings, the MN and MV cases, which are given in Fig. 13. As in HART the MV increased the noise radiation significantly (the reason will be shown later) while the MN setting at first glance does not reduce the noise level, however, the peak value is slightly reduced by 1.1dB. Obviously, the root input amplitude must be increased to obtain the larger noise gains measured in 1994 [16].

4.2 Blade pressures

The leading edge pressure sensors provide information about where a blade encounters a vortex in the plane of rotation. In Fig. 14 the distribution of 10/rev high-pass filtered leading edge pressures of one revolution is shown for the same range of flight path angles. The most intense blade-parallel BVI do occur at 6^o descent (d) in the first and fourth quarter of the disk as expected in this typical landing approach flight condition. The largest pressure fluctuations occur at the blade-parallel azimuth of $\psi = 45^o$ on the advancing side. On the retreating side, strong BVI is present at the tip around $\psi = 300^o$, which also has blade leading edge and vortex axis almost parallel to each other.

In climb, due to the nose-down inclination of

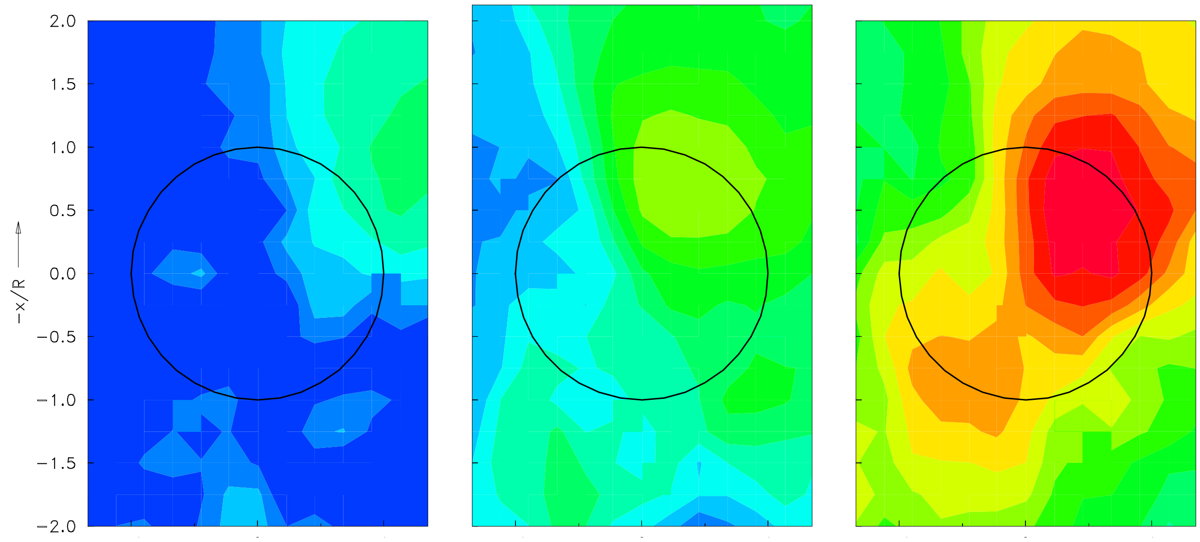

a) 6^o climb b) level flight c) 3^o descent

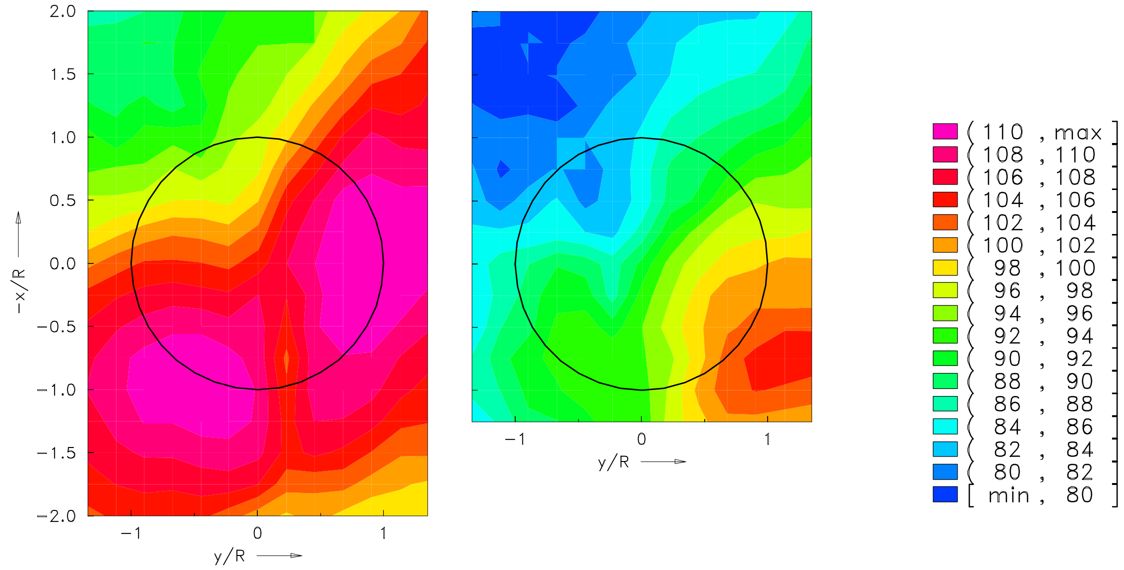

d) 6^o descent e) 12^o descent f) dB scale

Figure 12: Mid-frequency (8-40 bpf) noise radiation at different flight path angles.

the rotor, the vortices penetrate the disk very early and do only create oblique BVI which is not relevant for BVI noise (a). When tilting the rotor up, these BVI zones move downstream within the disk and in level flight (b) are around $\psi = 90^o$ and 270^o, where still a large angle exists between the vortex axis and the blade leading edge. In moderate descent condition (c) these BVI zones are coming close to blade-parallel BVI and do create significant related noise, which is maximum at 6^o descent (d). A steeper climb of 12^o with associated larger disk tilt backwards (e) causes the vortices to pass over most of the disk before penetrating it at the very end, which is not causing significant BVI noise any more. Again, this compares well with measurements during HART in 1994 [16], and verifies the conditions used as reference.

At the 6^o descent flight case, HHC at a frequency of 3/rev with an amplitude at the blade root of 0.8^o was applied during a phase sweep with increments of 30^o. As known from the HART test of 1994, two phases are of special interest: at $\psi_3 = 180^o$ the vibrations are at aminimum (MV) while at $\psi_3 = 300^o$ the noise radiation is minimized (MN). For both cases, the leading edge pressure fluctuations are given in Fig. 15 and the physics of HHC on BVI can be seen mainly in the first quadrant.

The MV case is intensifying the noise radiation significantly since the blade-parallel BVI events are intensified and additional shifted to the blade tip, where the local Mach numbers are larger (a). In contrast, the MN case shifts the BVI to more

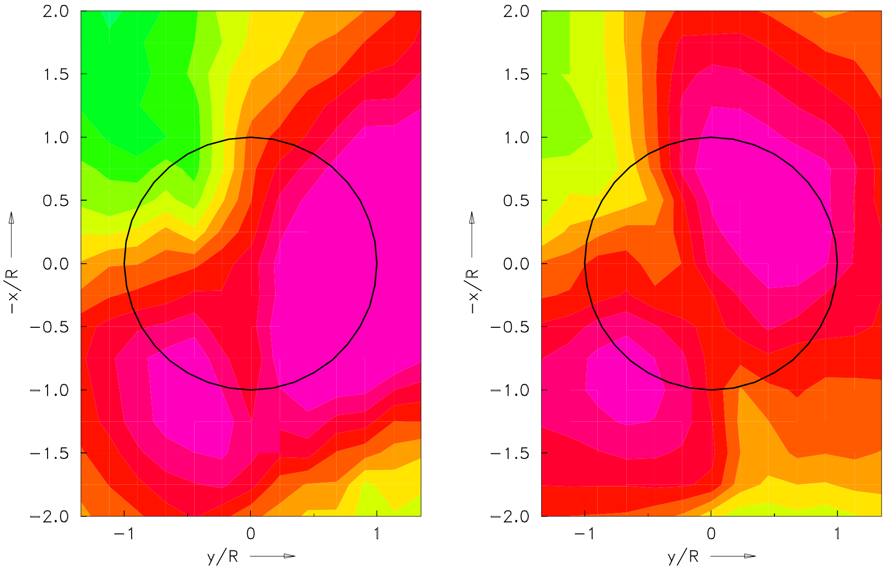

a) MV ($\psi_3 = 180^o$)   b) MN ($\psi_3 = 300^o$)

Figure 13: Mid-frequency (8-40 bpf) noise radiation at 6^o descent with 3/rev HHC, $\theta_3 = 0.8^o$, legend as in Fig. 12.

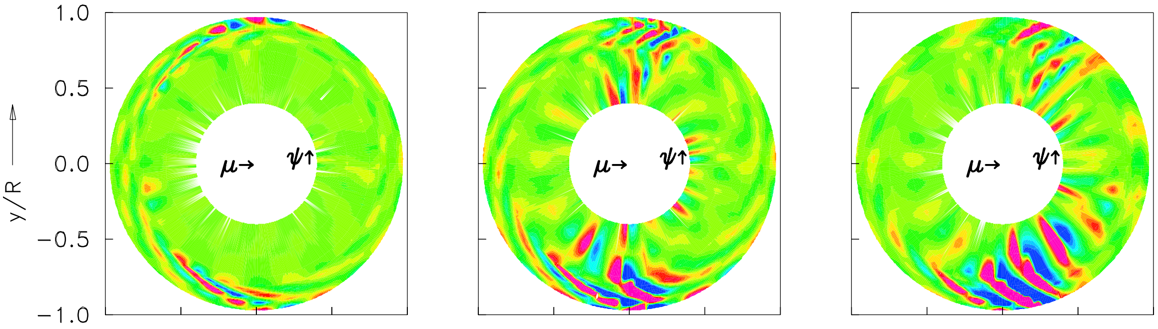

a) 6^o climb   b) level flight   c) 3^o descent

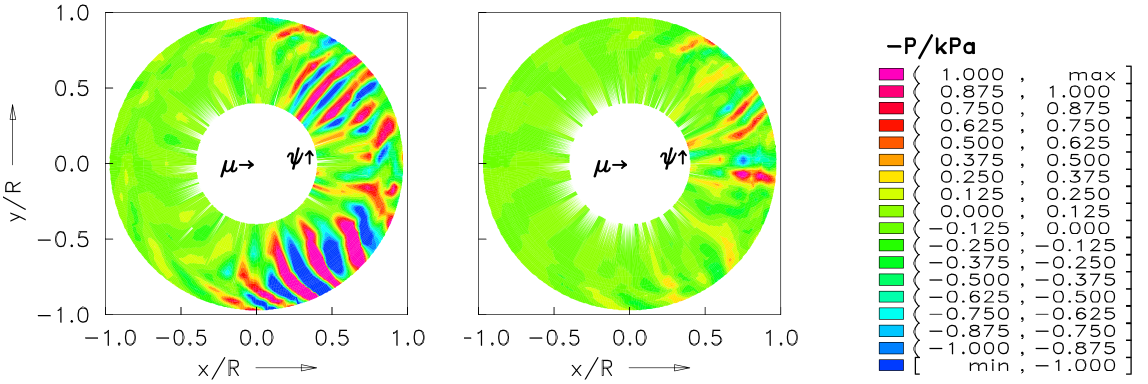

d) 6^o descent   e) 12^o descent   f) scale

Figure 14: Leading edge pressure distributions at different flight path angles, h.p. filtered at 10/rev.

inboard locations - at the outer radii the vortices are now located below the disk and do not cause BVI any more.

In Fig. 16 the low frequency content (i.e. loading due to dynamic pressure and blade motion: 0-10/rev) of the integrated chordwise blade pressure distribution is shown for the variation of flight path angles (a). At 6^o climb ($\triangle$) the loading is relatively homogeneous over the revolution. Beginning in level flight (+) the loading at the front of the disk ($\psi = 180^o$) drops and develops a strong 2/rev content, which is most visible in the 6^o (-) and 12^o desent ($\circ$) conditions.

When HHC is applied, a related 3/rev loading

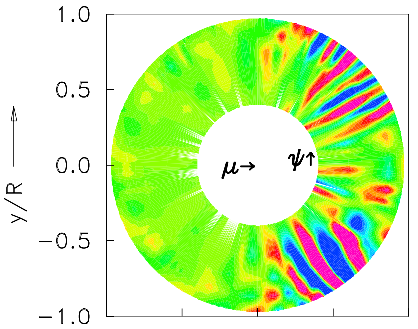

a) MV ($\psi_3 = 180^o$)

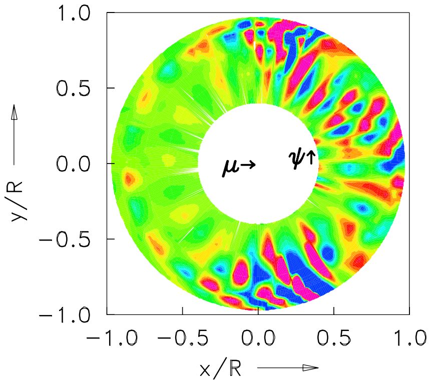

b) MN ($\psi_3 = 300^o$)

Figure 15: Leading edge pressure distributions at 6^o descent with 3/rev HHC, $\theta_3 = 0.8^o$, legend as in Fig. 14.

is superimposed on the BL case (b). In MN (△), the loading at $\psi = 120^o$ is increased and thus the strength of the vortex which later on interacts with the blade. Also, the downwash at this rotor area is increased which is known to convect the vortex below the disk. The same events are visible on the retreating side ($\psi = 240^o$). The MV (∘) case reduces the loading at the same locations, therewith weakening the vortex, but reducing the downwash, which will result in less convection.

The high frequency content (above 10/rev: BVI-induced loading) gives best indication of BVI intensity and location, and some insight into the mechanism of HHC. Fig. 17 shows the BL case without HHC (a) and the effect of MN (b) and MV (c) HHC settings. At BL, several BVI occur between 0^o and 75^o azimuth, with most intensity (or closest proximity to the blade) at slightly less than 60^o azimuth, where blade leading edge and vortex axis are almost parallel. Applying 3/rev HHC for minimum noise (MN, b) the strongest interaction increases significantly its intensity (an indication that the vortex is much stronger, which was found in Fig. 16), but the interaction location has moved to about $\psi = 70^o$, where the interaction angle between blade leading edge and vortex axis is larger, thus reducing the noise.

In the test of 1994 this interaction had moved even more (close to 90^o) and this explains the larger noise gains of that test, together with the larger HHC amplitude). The MV setting was found to shift the strongest interactions more outboard compared to the BL case, and to have less convection. Both is found in the high frequency signal: with less convection to the vortex remains in the disk, i.e. the intensity of the BVI's are almost constant for the entire sequence, and the magnitude is increased slightly. This results in the increased noise radiation.

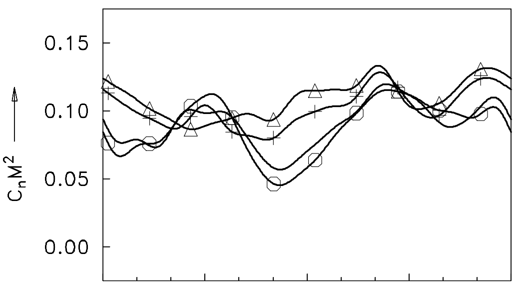

a) △: 6^o climb, +: level flight, −: 6^o descent, ∘: 12^o descent

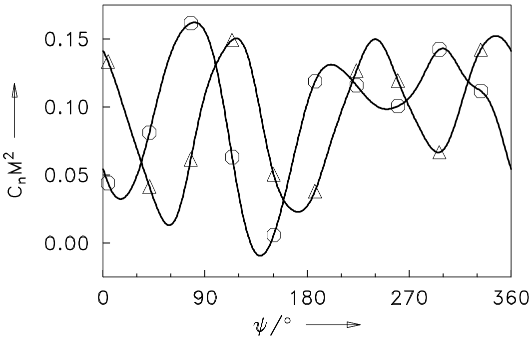

b) △: MN, ∘: MV

Figure 16: Blade aerodynamic loading at different flight path angles and HHC settings, $0.87R$, 0-10/rev l.p. filtered.

4.3 PIV results

The traverse of the PIV cameras was moved in a way that the visible flow swirl center was in the center of the images. The image center coordinates can thus be used as a first guess of the vortex center location, even if the final analysis identifies the center of the vortex some *cm* apart from this. An impression of the vortex flight path in a lateral plane of $y = 0.7R$ on the advancing side is given in Fig. 18 (a) for the BL case, together with the MN (red) and the MV case (blue). Also, the blade position at $\psi = 44^o$ and 136^o is plotted (at those azimuth the blade tip is at $y = 0.7R$), where the elastic deflections relative to the precone are already introduced. It can be seen that the elastic flap deflections due to HHC are very small compared to the vortex deflections, at least

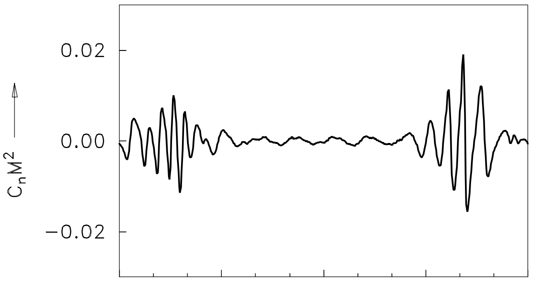

a) BL

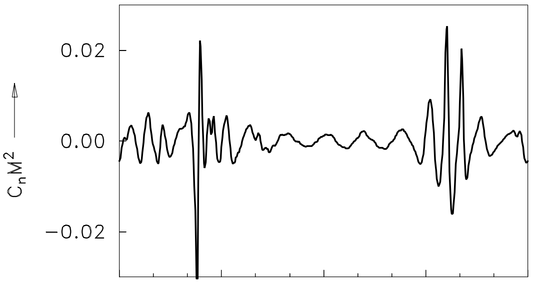

b) MN

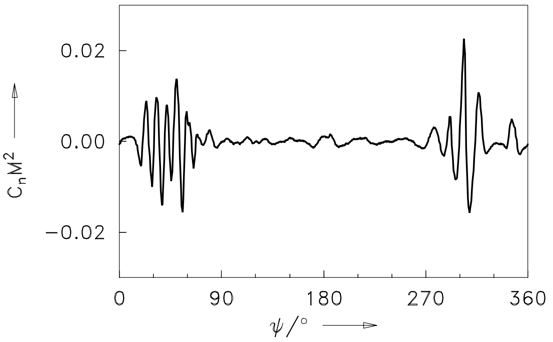

c) MV

Figure 17: Aerodynamic loading at MN and MV HHC settings, $0.87R$, 10/rev h.p. filtered.

at those azimuth.

Each symbol indicates a PIV measurement location; here these are 17a, 17, 18, 19, 20, 21, 22, 23, 55a, 55 of Fig. 10 for cases BL, MN, MV. To the left, where the vortices are created, the measurements are made in increments of $\Delta\psi = 5^o$ which is indicated by the high density of symbols. The BL case had a weak vortex, while the MN case had a strong vortex, and in the case MV no vortex was found - an indication for pure vorticity shed into the wake. In this case the first vortical structure was found much more downstream. Since the MV case creates a download at the tip in this blade position, a counter-rotating vortex was created right at the tip. The download is associated with an upwash, which can be seen in the flight path of this counterrotating vortex compared to the BL case. On the other hand, the MN case has a higher lift than the BL case, thus creates more downwash, which convects the vortex below the vortex flight path of the BL case. At typical BVI locations, this leads to the reduced noise radiation due to increased blade-vortex miss-distance.

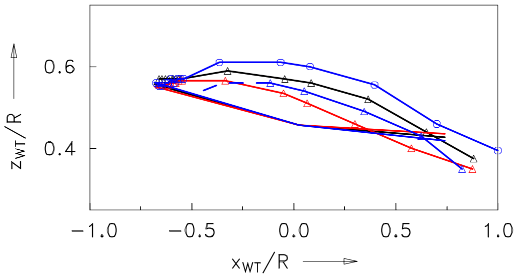

a) total view

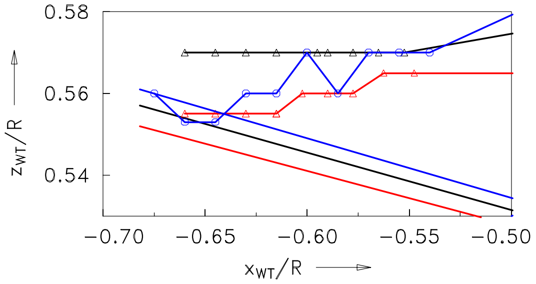

b) close-up view

Figure 18: PIV traverse coordinates as an indicator for the vortex flight path, $y = 0.7R$, $\alpha = 5.3^o$. black: BL, red: MN, blue: MV, △: conventional vortex, ∘: counterrotating vortex.

The vortex of “normal” sense of rotation in the MV case is created from the shed vorticity in between the maximum negative lift and the positive lift much more inboard, the dashed line in Fig. 18 (a) is an assumption of this. The creation location is below the counterrotating tip vortex, and both are traveling downstream as a pair. As a consequence, both do interact with the rotor blades in the first quadrant, which is one factor of increased noise radiation in this HHC case.

A close-up view of the vortex creation process (Fig. 18 b) already gives an interesting detail: while the BL case vortex is convecting horizontally (upwards relative to the tip path plane), the MN vortex (red) is convecting more upwards, which is caused by the stronger upwash of the vortex trailed by the blade before. Contrary, the MV case first convects down, which is originated by the opposite sense of rotation of the tip vortex here.

A result of processed PIV data at the locations 17-23 ($y = 0.7R$) of the BL case is given in Fig. 19 (a)-(g), tracing the vortex from creation down along its flight path through the rotor disk. The first image from the sequence of 100 taken at each location is shown and it must be kept in mind that there will be differences from revolution to revolution. The vorticity distribution

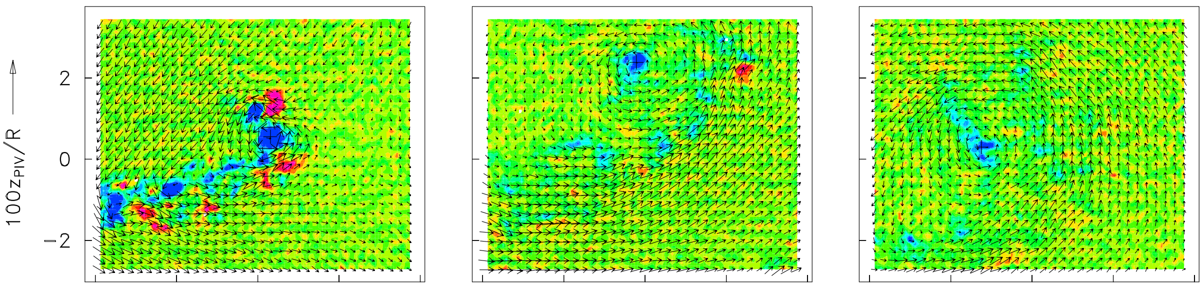

a) Loc. 17, $\psi_v = 0.071$ b) loc. 18, $\psi_v = 0.321$ c) loc. 19, $\psi_v = 0.571$

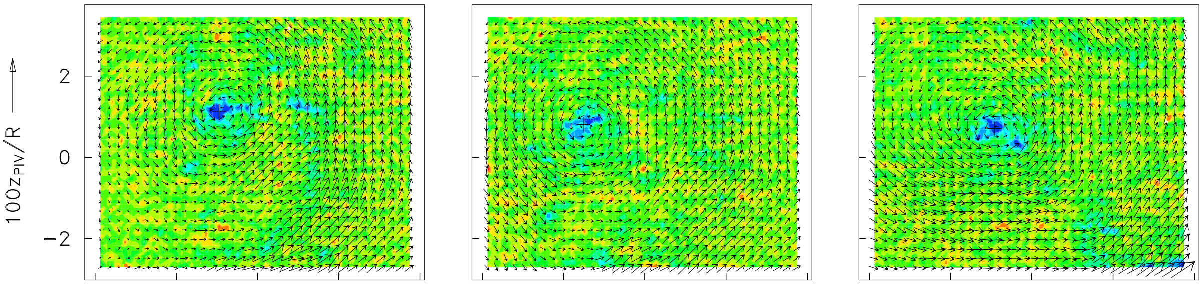

d) Loc. 20, $\psi_v = 0.682$ e) loc. 21, $\psi_v = 0.932$ f) loc. 22, $\psi_v = 1.182$

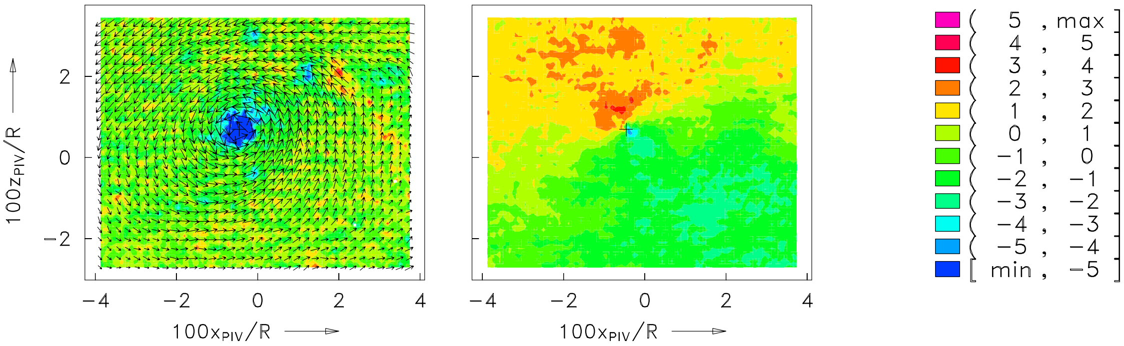

g) loc. 23, $\psi_v = 1.432$ h) loc. 23, crossflow i) scale

Figure 19: Vorticity development along the vortex flight path through the rotor disk, BL, $y = 0.7R$, vortex age ψ_v in 1/rev. Color coded: vorticity ω_y/Ω (a-g); corssflow component $100v/\Omega R$ (h)

$\omega_y = (\partial u/\partial z - \partial w/\partial x)/2$, computed from the vector fields and made non-dimensional by the rotational speed of the rotor, Ω, is color-coded in these figures and the vortex age from the time of release is given in fractions of a revolution.

Shortly after its creation there is a lot of distributed vorticity present in the wake behind the trailing edge (a) and the tip vortex cannot always be clearly identified. A quarter revolution later (b) vorticity is significantly diminished. Here, the center of the vortex is quite close to the upper image border line, which indicates that the vortex had a certain movement from one image to the next and that at this stage the swirl center was not always as easy to be identified in the camera raw data images like that shown in Fig. 9. Especially the BL case has a small radial lift gradient at the azimuth of this vortex emission and the PIV raw data rather showed a band of vorticity than a concentrated vortex. With growing age of the vortex this became better (c)-(e), and at the rear of the disk the vortex was completely rolled-up (f) and (g). The black + sign indicates where the center of vorticity is computed.

In these figures, only each third vector is plotted, so the net spatial resolution is 1.5mm between two vectors. Due to the high quality of the laser and seeding density, no outliers were found during the analysis. This indicates the possibility to further reduce the size of the analysis interrogation windows, which here had 24*24 pixels, and thus to increase the spatial resolution of the results.

The crossflow distribution of location 23 is given in Fig. 19 (h). It can be seen that there is a global gradient in crossflow from the top to the bottom and a smaller one from the left to the right. A strong local component can be found at the center of the vortex (at the + sign) which indicates the vortex axial velocity whithin its core. The global gradients indicate that the vortex was not cut orthogonal by the laser light sheet and can be used to rotate the field of velocity vectors into a plane normal to the vortex axis, where no crossflow gradients exist outside the vortex.

4.4 SPR results

The analysis of SPR results requires some post-processing since the data contain only positions of the markers along leading and trailing edge in space, i.e. in the wind tunnel coordinate system. The goal are flap, lead-lag and torsion displacements of the quarter chord line in the shaft coordinate system with origin in the center of the hub. To obtain these results, the position of the hub center must be known (which turned out not to be an easy task), and the exact shaft angle of attack, measured at the rotor balance. To reduce measurement noise, higher order polynomials are carefully fitted through the positions of the leading and trailing edge markers, interpolated to the quarted chord line and differenciated to get the local pitch. Using the build-in pre-twist and the measured blade root pitch angle, the pure elastic pitch deformation can be computed.

In Fig. 20 the time history of the blade tip flapping displacement is shown for the variation of flight path angles (a) and the two HHC cases (b). In climb and descent a 2/rev flapping motion is present which is smaller at the steep descent. When 3/rev HHC is applied (cases MN and MV), a 3/rev flapping dominates the figure as expected. The amplitudes are about 1%R which is about 20mm at the tip.

The radial distributions of the BL and HHC cases are given for six azimuth positions in Fig. 21. Up to 0.5R the differences between the BL and HHC cases are small, but outside the elastic bending due to HHHC is clearly visible. When symbols are missing, the appropriate markers blew off the surface and were replaced later on. A best fit to the markers was only possible with a polynomial of 4th order in r, which indicates that higher order blade bending mode shapes are creating these elastic deformations and not only the first flap bending mode.

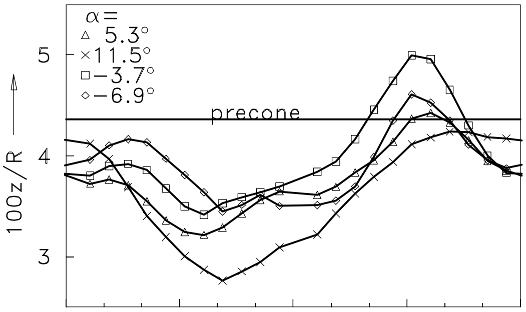

a) α-sweep

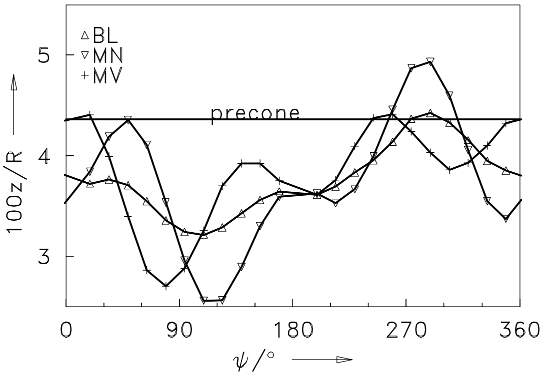

b) HHC cases

Figure 20: Flap displacement at the blade tip, α-sweep and HHC cases.

The local pitch can either be computed by the vertical differences of the leading and trailing edge marker pairs, or from the polynomial representation of these. The first method increases the errors while the latter smoothes irregularities. The results presented for torsion thus are computed from the polynomial representation of the marker displacements. Fig. 22 shows the elastic blade tip torsion for the α-sweep (a) and the HHC cases MN and MV (b). As is the case in the flapping motion a 2/rev oscillation is visible in the torsion, which reduces in climb. The peak values around $\psi = 270^o$ in the curves of $\alpha = -3.7^o$ and -6.9^o are due to extrapolation and shall be ignored (the outer marker pairs were not useful at these positions).

With 3/rev HHC a strong 3/rev torsion is the response which was expected due to the natural frequency in torsion at 3.6/rev of this rotor. It clearly can be seen that the MN case has a higher pitch at $\psi = 135^o$, where the vortex is created that later on interacts with the blade. This higher loading creates a stronger downwash for the vortices passing this area which convect accordingly more downwards below the blade, which increases the blade-vortex mis-distance and thus reduces noise. The MV case has almost opposite behavior, the strong nose-down pitch at this region even creates tip vortices of opposite sense of rotation due to download at the tip. More inboard the loading changes its sign and a conventional secondary vortex is created. Both of them were captured and measured by PIV.

It may be noted that also the MN case creates a counterrotating tip vortex, but in another area around 180^o azimuth. At $r = 0.4R$ this vortex also was measured in HART II.

5 Conclusions

In this paper, the HART II test in the LLF of the DNW was described and some results have

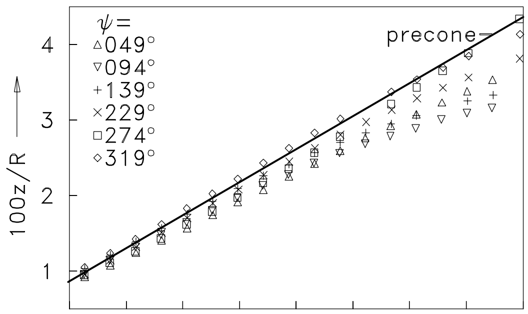

a) BL case

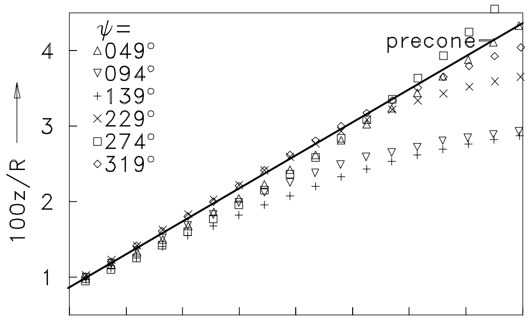

b) MN case

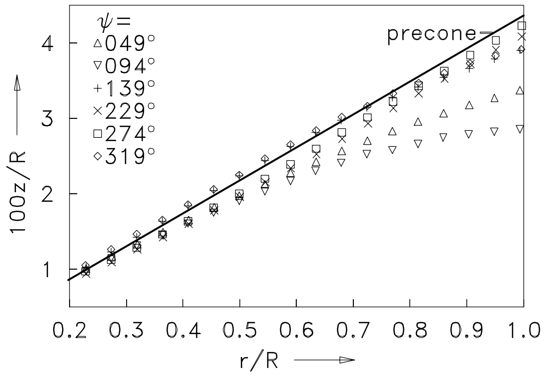

c) MV case

Figure 21: Radial flap displacement, BL and HHC cases.

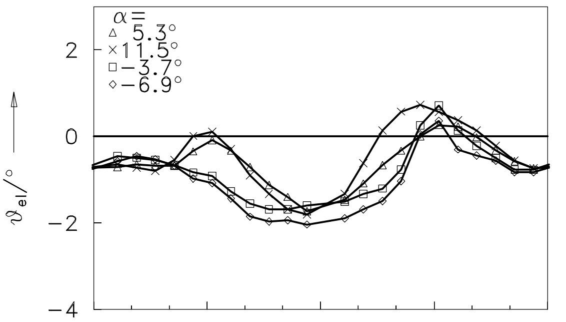

a) α-sweep

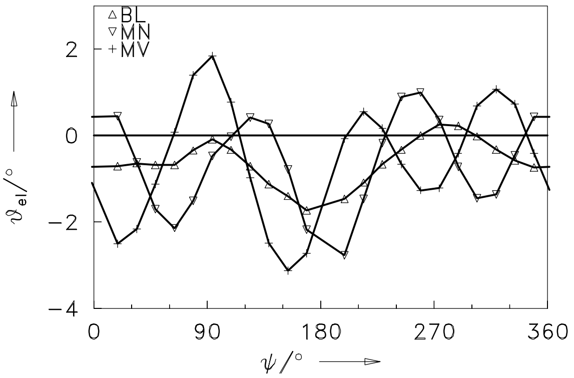

b) HHC cases

Figure 22: Elastic torsion at the blade tip, α-sweep and HHC cases.

been shown. An international cooperative effort led to a very comprehensive and unique data base for rotor wake modeling and code validation, featuring all necessary information needed: acoustics, aerodynamics, blade motion and an extraordinary amount of flow data. Based on this it is expected that data analysis and modeling provides the basis for significant improvements of rotor aeromechanics simulation and noise prediction. The HART II team will stay together to analyse all these data which is as chellenging as the conduction of the test itself.

Acknowledgement

An international test as complex as HART II requires a lot of engagement of all participants, both in the fore- and in the background. It would fill pages to name everybody. Instead, the teams are specifically addressed. These are: the prediction team, the test team and the management team, all of them consisting of US/French/German members working years ahead in real partnership preparing the rotor hardware, the measurement techniques, the test matrix and the funding. Specificially the funding of the test from US and French side, the development of 3C-PIV and preparation of the rotor and conduction of the test on DLR side shall be mentioned, and the strong support of DNW during the test. Without the enthusiasm of all of them this test would never have come true - thanks to all of them!

References

[1] W.R. Splettstößer, R. Kube, U. Seelhorst, W. Wagner, A. Boutier, F. Micheli, *Higher Harmonic Control Aeroacoustic Rotor Test (HART) - Test Documentation and Representative Results -,* DLR IB 129-95/28, Braunschweig, Germany, 1995

[2] P. Beaumier, P. Spiegel, *Validation of ONERA Prediction Methods for Blade-Vortex Interaction using HART Results,* 51st An-

nual Forum of the American Helicopter Society, Fort Worth, TX, USA, 1995

[3] B.G. van der Wall, *Vortex Characteristics Analysed from HART Data,* 23rd European Rotorcraft Forum, Dresden, Germany, 1997

[4] P. Beaumier, P. Spiegel, *Validation of ONERA Prediction Methods for Blade-Vortex Interaction using HART Results,* 51st Annual Forum of the American Helicopter Society, Fort Worth, TX, USA, 1995

[5] T.F. Brooks, D.D. Boyd, C.L. Burley, J.R. Jolly, *Aeroalastic Codes for Rotor Harmonic and BVI Noise - CAMRAD.Mod1/HIRES,* 2nd AIAA/CEAS Aeroacoustics Conference, State College, PA, USA, 1996

[6] B.G. van der Wall, M. Roth, *Free-Wake Analysis on Massively Parallel Computers and Validation with HART Test Data,* 53rd Annual Forum of the American Helicopter Society, Virginia Beach, VA, USA, 1997

[7] B.G. van der Wall, *Simulation of HHC on Helicopter Rotor BVI Noise Emission using a Prescribed Wake Method,* 26th European Rotorcraft Forum, The Hague, Netherlands, 2000

[8] Y. Yu, *The HART II Test - Rotor Wakes and Aeroacoustics with Higher-Harmonic Pitch Control (HHC) Inputs - The Joint German/French/Dutch/US Project -,* 58th Annual Forum of the American Helicopter Society, Montreal, Canada, 2002

[9] M. Raffel, H. Richard, G. Schneider, F. Klinge, K. Ehrenfried, K. Pengel, G. Feenstra, *Recording and Evaluation Methods of PIV Investigation on a Helicopter Rotor Model,* 11th International Symposium on Laser Applications to Fluid Mechanics, Lissabon, Portugal, 2002

[10] K. Pengel, R. Müller, B.G. van der Wall, *Stereo Pattern Recognition - the Technique for Reliable Rotor Blade Deformation and Twist Measurement,* AHS International Meeting on Advanced Rotorcraft Technology and Life Saving Activities, Utsunomiya, Tochigi, Japan, 2002

[11] B. Gelhaar, B. Junker, W. Wagner, *DLR - Rotor Teststand Measures Unsteady Rotor Aerodynamic Data,* 19th European Rotorcraft Forum, Cernobbio, Italy, 1993

[12] U. Seelhorst, K.A. Bütefisch, K.H. Sauerland, *Three Component Laser-Doppler Velocimeter Development for Large Wind Tunnel,* ICIASF '93 Record, pp.33.1-33.7, 1993

[13] A. Boutier, J. Lefèvre, F. Micheli, *3D Laser Velocimetry and Blade Tip Attitude Measurements by TART Method within the HART Test Program,* ONERA RTS 5/51432 PY, Chatillon, France, 1996

[14] M. Raffel, C. Willert, J. Kompenhans, *Particle Image Velocimetry, A Practical Guide,* Springer, ISBN 3-540-63683-8, 1998

[15] W.R. Splettstößer, G. Niesl, F. Cedenese, F. Niti, D.G. Papanikas, *Experimental Results of the European HELINOISE Aeroacoustic Rotor Test in the DNW,* 19th European Rotorcraft Forum, Cernobbio, Italy, 1993

[16] W.R. Splettstößer, R. Kube, U. Seelhorst, W. Wagner, A. Boutier, F. Micheli, E. Mercker, K. Pengel, *Key Results from a Higher Harmonic Control Aeroacoustic Rotor Test (HART) in the German-Dutch Wind Tunnel,* 21st European Rotorcraft Forum, Saint-Petersburg, Russia, 1995